Core energies of dislocations in bcc metals

N. Bertin, W. Cai, S. Aubry, and V. V. Bulatov

Phys. Rev. Materials **5**, 025002 — Published 24 February 2021

DOI: 10.1103/PhysRevMaterials.5.025002

Core energies of dislocations in BCC metals

N. Bertin[1,*], W. Cai[2], S. Aubry[1], and V.V. Bulatov[1]

[1]Lawrence Livermore National Laboratory, Livermore, CA, USA
[2]Department of Mechanical Engineering, Stanford University, Stanford, CA, USA
[*]Corresponding author: bertin1@llnl.gov

February 5, 2021

Abstract

Accurate methods and an efficient workflow for computing and documenting dislocation core energies are developed and applied to $\frac{1}{2}\langle 111\rangle$ and $\langle 100\rangle$ dislocations in five body-centered cubic (BCC) metals W, Ta, V, Mo, and α-Fe represented by 13 model interatomic potentials. For each dislocation type, dislocation core energies are extracted for a large number of dislocation characters thoroughly sampling the entire 2-space of crystallographic line orientations of the BCC lattice. Of particular interest, core energies of the $\frac{1}{2}\langle 111\rangle\{110\}$ dislocations are found to be distinctly asymmetric with respect to the sign of the character angle, whereas core energies of $\langle 100\rangle\{110\}$ junction dislocations exhibit marked cusps for line orientations vicinal to the closed-packed $\langle 111\rangle$directions. Our findings furnish substantial new insights for developing accurate models of dislocation core energies employed in mesoscale Dislocation Dynamics simulations of crystal plasticity.

Keywords – Core energy, Molecular Dynamics, BCC metals, Non-singular elasticity

1 Introduction

Just like for any other crystal defect, energy of a lattice dislocation is its most basic physical characteristic bearing on most if not all of the observed dislocation behaviors. In particular, dislocation energy defines configurational driving forces for dislocation microstructure evolution [1, 2], governs dislocations mobility [3] and decides outcomes of dislocation reactions such as formation of dislocation junctions that play a fundamental role in work-hardening [4–6].

It is possible and useful to partition the dislocation energy into its elastic energy and core energy components. Sufficiently far away from a dislocation line, its effect on the surrounding lattice is accurately described by the standard linear elasticity theory in which the dislocation is viewed as a line source of lattice distortion. On approaching the line closer, lattice distortions increasingly deviate from the elastic theory predictions. Accuracy of linear elasticity predictions at intermediate distances can be and has been improved by considering the dislocation to be a distributed source of elastic fields rather than a

mathematical line. Either intrinsic to the dislocation itself or induced by its interaction with other dislocations, momenta of the dislocation source distribution or elastic *core fields* can be calibrated to accurately describe lattice distortions at intermediate distances thus bringing the range of applicability of linear elasticity closer to the dislocation line [7–9]. Whether the standard line source or a distributed source model is assumed, at still shorter distances lattice discreteness becomes increasingly evident and lattice distortions become too large for linear elasticity to apply. Dislocation core can be thought of as a tube of material of radius w coaxial with the dislocation line such that linear elasticity holds outside the tube but breaks down in its interior.

Subject to restrictions discussed below, energy of a generally shaped dislocation line or of a group of interacting dislocations can be accurately predicted if the elastic-core partitioning is known for some standard reference configuration, such as for the simple case of an infinite straight dislocation. In other words, core energy computed for a straight dislocation should be *transferable* to arbitrarily curved dislocations. One necessary condition for such a transfer to be accurate is that curvature radii of and distances R between dislocation lines are greater than the core radius[1], $R \gg w$. Under such conditions, dislocation energy is well approximated as the integral of the core energy taken along the dislocation lines plus the energy of elastic lattice distortions integrated over the crystal volume outside dislocation cores [10]. Accuracy of such an energy transfer is controlled by the ratio w/R and the transfer becomes asymptotically exact in the limit where energy partitioning is performed at $R \to \infty$. Condition $R \gg w$ is obviously violated whenever dislocation line orientation changes abruptly, such as at a corner formed by dislocation cross-slip or at a junction node (here $R = 0$). It would take additional parameters to correctly account for energy associated with such configurations which are outside the scope of this work. Another important conditions for the transfer to remain accurate is that a correct version of elasticity theory is used both for partitioning and for transfer. As a corollary, the often practiced use of isotropic linear elasticity for computing elastic energy of dislocations in an elastically anisotropic crystal, constitutes an uncontrolled approximation.

One standard reference configuration often used for computing and partitioning or extraction of dislocation energies is that of a single infinite straight dislocation inserted into a cylinder made of an otherwise perfect crystal. The dislocation is assumed inserted along the cylinder axis. The total energy E^{tot} associated with the dislocation is partitioned into an elastic and a core contribution

$$E^{\mathrm{tot}} = E^{\mathrm{el}} + E^{\mathrm{core}} \tag{1}$$

The energy contained in the inner cylinder of radius w centered on the dislocation is the core energy $E^{\mathrm{core}}(w)$. Then the elastic energy $E^{\mathrm{el}}(w)$ is equal to the elastic strain energy induced by the dislocation in the entire crystal volume outside the core. Assuming the crystal is elastically isotropic, the elastic energy per unit length of a straight dislocation is [11]:

$$E^{\mathrm{el}}(w) = \frac{\mu b^2}{4\pi}\left(\cos^2\theta + \frac{\sin^2\theta}{1-\nu}\right)\ln\left(\frac{R}{w}\right) \tag{2}$$

[1]We assume that core radius w is sufficiently large to fully subsume contributions of the intermediate-range elastic core fields into the core energy.

where μ and ν are the shear modulus and Poisson ratio of the crystal, θ is the angle between the dislocation line and its Burgers vector of magnitude b, and R is the outer radius of the cylinder. It is possible to partition the same total energy differently, e.g. by increasing the radius of the inner cylinder to $r_c > w$ and thus subsuming some of the energy previously counted as elastic into the core component

$$E^{\text{tot}} = E^{\text{core}}(r_c) + \frac{\mu b^2}{4\pi}\left(\cos^2\theta + \frac{\sin^2\theta}{1-\nu}\right)\ln\left(\frac{R}{r_c}\right) \tag{3}$$

Formally, the above balance equation is invariant with respect to changing core radius from w to arbitrary r_c and simultaneously modifying the core energy as follows

$$E^{\text{core}}(r_c) = E^{\text{core}}(w) + \frac{\mu b^2}{4\pi}\left(\cos^2\theta + \frac{\sin^2\theta}{1-\nu}\right)\ln\left(\frac{r_c}{w}\right) \tag{4}$$

The above invariance holds irrespective of the magnitude of reference radius r_c that can be chosen to be smaller than the physical spread of the core w or exceed the outer radius R of the cylinder. Although $r_c = b$ is a popular choice, the value of r_c is arbitrary. For as long as the core energy and the elastic energy are both computed or *referenced* at the same r_c, partitioning is correct and the total energy remains the same. And since it is only the total energy of a dislocation that constitutes a physically measurable quantity, the core energy can be *documented* by reference to arbitrary r_c. Full documentation of the core energy should also include the elastic constants, e.g. μ and ν, used in partitioning. For transferability, the same elastic constants should be employed in any subsequent use of the so-extracted core energy data.

Dislocation energies are computed using atomistic models ranging in fidelity from simple and computationally efficient interatomic potentials [12–14] to sophisticated and costly *ab-initio* calculations [8,15]. When extracted using Eq. (3) or another appropriate partitioning method and referenced at $r_c = b$, dislocation core energies are typically in the range of several tenths of eV/Å in body-centered cubic (BCC) [12,13] and face-centered cubic (FCC) [14, 16, 17] metals. Core energy of a dislocation is known to depend on its line orientation commonly quantified by the angle between its tangent vector and the Burgers vector and often referred to as dislocation character. A single angle is obviously insufficient since two parameters are needed to fully define a line orientation in space whereas the familiar dislocation character angle only specifies the line direction within the crystallographic plane that contains the Burgers vector. Because there are multiple planes containing the Burgers vector, the specific plane in which the character angle is defined is often implied but only rarely stated explicitly. Such traditional use is appropriate in the context of FCC and, to a lesser extent, in hexagonal (HCP) crystals where dislocations are nearly exclusively confined to a specific set of planes: {111} planes in FCC and basal, prismatic or pyramidal planes in HCP. However in crystals with the BCC lattice that are of primary interest in this work, dislocations can reside and glide in {110}, {112}, {123} and possibly other planes of the ⟨111⟩ zone [18] thus making necessary to extend the notion of dislocation character and to quantify dislocation properties in the full orientation space. One option is to use Miller index of a crystallographic orientation parallel to the dislocation line. We use such a description on occasion, but prefer to retain the traditional in-plane dislocation character and just add another parameter to specify the plane orientation. To be referred to as *zonal*

character, plane orientation can be defined by its Miller index or by the dihedral angle ϕ it forms with a specific crystallographic plane of the same Burgers vector zone. In the following we use the convention that the zonal angle ϕ for the $\frac{1}{2}[111]$ dislocation is defined as the dihedral angle between the reference $(\bar{1}10)$ zonal plane and the plane formed by the dislocation line vector and its Burgers vector. Likewise, the zonal angle is defined with respect to the reference (100) plane for the $\langle 001 \rangle$ dislocation. Given that, in principle, a dislocation can glide (move conservatively) in any plane of its Burgers vector zone, we will also refer to the same zonal planes as glide planes.

This paper presents an efficient workflow for extracting accurate core energies from atomistic calculations, carefully documents core energies computed for five BCC metals W, Ta, V, Mo and α-Fe in a wide range of dislocation orientations in the full orientation 2-space, and describes how such data can be transferred to predict energies of arbitrary dislocation configurations. Although our primary focus in this work is on method development, we report a number of results and observations of potential physical significance that have not been reported before. Among them is asymmetry of the core energy of the $\frac{1}{2}\langle 111 \rangle$ dislocations with respect to the in-plane character angle and a sharp cusp in the core energy of $\langle 001 \rangle$ junction dislocations at $\theta = \pm 54.74^\circ$ in-plane character angle in the $\{110\}$ planes.

The paper is organized as follows. Section 2 describes our methods for computing and extracting core energies from atomistic calculations in the context of classical isotropic and anisotropic singular elasticity. Our main findings on dislocation core energies are then presented and discussed in Section 3 focusing on tungsten as a representative BCC metal. Section 4 describes how our documented core energies can be subsequently re-used in predicting dislocation energies within recently developed isotropic and anisotropic non-singular models of dislocations. Section 5 documents core energies computed for five BCC metals W, Ta, V, Mo and α-Fe respresented by 13 different interatomic potential models. Finally, section 6 presents a summary.

2 Methods

Rather than considering a single dislocation as described in the introduction, here we employ a method in which the dislocation core energy is extracted from the total energy of a dislocation dipole [13]. To compute the energy, a dislocation dipole is introduced in a 3D-periodic supercell with repeat vectors $\boldsymbol{c}_1$, $\boldsymbol{c}_2$, and $\boldsymbol{c}_3$. Two dislocations of the dipole are perfectly straight and parallel to each other and to the supercell vector $\boldsymbol{c}_3$ thus making the dislocations infinite. Use of 3D periodic boundary conditions ensures that the model crystal contains no surfaces or any other unwanted interfaces that, if left unaccounted, can negatively impact accuracy of core energy calculations [1]. At the same time, full 3D periodicity means that, rather than dealing with just one primary dislocation dipole, the crystal contains an infinite 2D super-lattice of dislocations dipoles, one dipole in each periodic replica of the supercell.

In this work calculations of core energies are limited to zero temperature, but for non-zero temperatures the logic remains the same. Once relaxed to its minimum, the energy of the atomistic model E^{atm} is broken down into the following four components the last three of which are then computed separately

$$E^{\text{atm}} = 2E^{\text{core}}(r_c) + E^{\text{prm}}(r_c) + E^{\text{img}} + NE^{\text{coh}} \tag{5}$$

Here, $2E^{\text{core}}$ is twice the core energy[2], E^{prm} is the elastic energy of the primary dipole, E^{img} is the interaction energy between the primary dipole and its periodic images, E^{coh} is the per atom energy of a perfect crystal, and N is the number of atoms in the crystal. Of the four terms on the right hand side, E^{coh} is either known in advance or readily computed whereas image interaction energy E^{img} is computed following the accurate and efficient regularization method developed in [13]. After subtracting E^{img} and NE^{coh} from E^{atm}, the remaining two terms is the energy of an isolated (no images) dislocation dipole written as a sum of its elastic and core components.

To extract the core energy, the elastic energy of a dislocation dipole in an infinite isotropic elastic solid can be accurately computed as

$$\begin{aligned} E^{\text{prm}}_{\text{iso}}(r_c) = {} & \frac{\mu}{2\pi}(\boldsymbol{b}\cdot\boldsymbol{\xi})^2 \ln\left(\frac{R}{r_c}\right) \\ & + \frac{\mu}{2\pi(1-\nu)}(\boldsymbol{b}\times\boldsymbol{\xi})\cdot(\boldsymbol{b}\times\boldsymbol{\xi})\ln\left(\frac{R}{r_c}\right) \\ & + \frac{\mu}{2\pi(1-\nu)}\frac{1}{R^2}\left[(\boldsymbol{b}\times\boldsymbol{\xi})\cdot\boldsymbol{R}\right]^2 \end{aligned} \tag{6}$$

where $\boldsymbol{b}$ is the Burgers vector, $\boldsymbol{\xi}$ is a unit (tangent) vector parallel to the dislocations, $\boldsymbol{R}$ is the shortest vector connecting two dislocations of the dipole and R is the magnitude of the same vector. As was previously pointed out [15], a common mistake in extracting core energies from the energy of a dislocation dipole has been rooted in ignoring the fact that, in general, the elastic energy of a dislocation dipole depends on the dipole orientation with respect to the host crystal. The latter dependence is correctly accounted for by the last term in Eq. (6) where unit vector $\boldsymbol{R}/R$ defines the dipole orientation.

A corresponding semi-analytical expression for the dipole energy in a generally anisotropic solid was previously obtained by integrating Stroh's solution for the stress fields [13] induced by two dislocation leading to:

$$E^{\text{prm}}_{\text{aniso}}(r_c) = \sum_{n=1}^{3} \text{Re}\left[\frac{1}{2\pi i}h_1(n)\ln\left(\frac{x+p_n y}{r_c}\right)\right] \tag{7}$$

where $\text{Re}\,[\cdot]$ is the real part of a complex number, i is the imaginary unit, x and y are the components of the separation vector $\boldsymbol{R}$ in the plane orthogonal to the dipole, and p_n are the roots of Stroh's sextic equation. $h_1(n)$ is a function that depends on p_n, the elastic constants, and the Burgers vector $\boldsymbol{b}$ of the dipole (see [13] for more details). If desired, the above expression can be re-written in a frame independent form similar to Eq. (6).

For each dipole, two straight dislocations with opposite Burgers vectors are initially inserted along supercell vector $\boldsymbol{c}_3$ and separated by $\boldsymbol{R} = \boldsymbol{c}_2/2$. Energy of the resulting atomistic configuration is then carefully minimized and the lowest achieved energy value

[2]This implies that structure and energy of two dislocation cores in the dipole are the same which should hold for BCC crystals owing to the inversion centro-symmetry.

is taken as E^{atm}. Sometimes (often in this series of calculations) in the course of energy minimization one or both dislocations shift from their intended initial positions likely owing to the elastic interaction between two primary dislocations and their interactions with the image dislocations. If left undetected or unaccounted, such shifts may cause significant errors in computing the image interaction term and the primary dipole energy term in Eq. (5) and may result in unacceptable errors in the extracted core energies. Any such shift can be detected using one of the methods available in the literature, e.g. the dislocation extraction algorithm [19]. The resulting corrected separation vector $\boldsymbol{R}$ should be used instead of $\boldsymbol{c}_2/2$ for computing the elastic energy terms.

Whereas the length of supercell vector $\boldsymbol{c}_3$ is dictated by the lattice period along each given dislocation line orientation (and the interatomic potential cutoff radius for low-index orientations), vectors $\boldsymbol{c}_1$ and $\boldsymbol{c}_2$ should be selected to ensure that cores of the primary dipole dislocations and those of the image dislocation do not overlap. Thus, both vectors should be long enough to ensure that all dislocations are at least at a distance $2w$ apart from each other. In reality, it is not obvious in advance what the physical spread of the core is. Consequently, for each model potential and each dislocation line orientation the core energy is computed in this work in four supercells of different dimensions. It was noted in [12] that, depending on elastic anisotropy, "ideal" aspect ratios may exist for which the image interaction energy term either vanishes or is greatly reduced. Although possibly useful for reducing the overall error, we note that such ideal aspect ratios are predicted to exist only for elastically anisotropic solids. Furthermore, for solids with weak and moderate anisotropy, the ideal aspect ratios can be unacceptably large. In all calculations reported here, aspect ratio $\boldsymbol{c}_2/\boldsymbol{c}_1$ was kept approximately constant at ~ 1.5 by selecting supercell vectors $\boldsymbol{c}_1$ and $\boldsymbol{c}_2$ to be multiples of two shortest mutually orthogonal lattice vectors perpendicular to the crystallographic orientation of the dislocation line.

Although it is important to keep dislocations well separated, in our experience core energies extracted from very large supercells are prone to errors unrelated to non-linear effects in the dislocation core. First, both the elastic energy of the primary dipole and the image interaction energy term increase logarithmically with increasing supercell dimensions. Thus, since the core energy is obtained by subtracting two large floating-point numbers for E^{prm} and E^{img} from another large floating-point number for E^{atm}, numerical round-off errors can become intolerable in supercells of very large dimensions. Additionally, standard methods for non-linear minimization, e.g. conjugate gradient, are known to suffer from ill-conditioning when trying to minimize the energy of a large atomistic model. Ill-conditioning may cause energy minimization to terminate prematurely resulting in an unacceptable error in E^{atm} thus directly translating into an error in the extracted core energy. Based on our earlier experiences with dislocation core energy calculations, all atomistic calculation were performed in supercells with the initial dipole separation vector $\|\boldsymbol{R}\|$ ranging from ~ 50 to 150Å.

We computed E^{atm} for five BCC metals – tungsten, tantalum, molybdenum, vanadium, and iron – modeled with 13 interatomic potentials of the embedded atom method (EAM) type listed in Table 1. Even though most parameters entering the partitioning equation (5) have been previously reported in the literature, to minimize errors of core energy extraction we pre-computed the same parameters again. As shown in Table 1, anisotropy ratios A of three models representing tungsten are all close to 1.0 thus making Eq. (6) appropriate

Metal	Potential	b (Å)	E^{coh} (eV/atom)	C_{11} (GPa)	C_{12} (GPa)	C_{44} (GPa)	A
W	Zhou et al. [20]	2.7408	-8.759988337077914	521.84	203.85	160.74	1.01
W	Olsson [21]	2.7366	-8.900004790205685	531.50	204.47	163.11	1.00
W	Juslin et al. [22]	2.7411	-8.899995957111060	520.15	198.62	156.85	0.98
Ta	Li et al. [23]	2.8602	-8.089000065284608	248.92	144.27	86.53	1.65
Ta	Zhou et al. [24]	2.8601	-8.090001526987180	263.65	157.82	81.16	1.53
V	Olsson et al. [21]	2.6240	-5.310000188013802	231.75	119.09	45.96	0.82
V	Han et al. [25]	2.6241	-5.300000227940302	226.34	119.09	43.22	0.81
Mo	Ackland and Thetford [26]	2.7256	-6.819999932888322	467.43	161.14	108.89	0.71
Mo	Zhou et al. [24]	2.7281	-6.809997810402422	456.04	166.22	113.10	0.78
Fe	Ackland et al. [27]	2.4825	-4.316000049472621	242.97	144.89	116.08	2.37
Fe	Mendelev et al. [28]	2.4728	-4.122435100730854	243.58	144.88	116.02	2.35
Fe	Zhou et al. [24]	2.4820	-4.289994344756849	229.60	135.27	116.75	2.48
Fe	Chamati et al. [29]	2.4825	-4.280000069342009	241.12	146.65	114.03	2.41

Table 1: List of metals and properties of the potentials used for the extraction of core energies in this work. To minimize errors in subsequent core energy extraction, all listed quantities were pre-computed at zero temperature rather than taken from the literature. The anisotropic ratio $A = 2C_{44}/(C_{11} - C_{12})$ is given in the last column.

to use for the same three models. However for uniformity we used the general anisotropic expression, Eq. (7), to compute the elastic energy terms and to extract dislocation core energies in all 13 models.

To thoroughly sample the dislocation orientation space we opted to place dislocations into three zonal planes $\{110\}$, $\{112\}$, and $\{123\}$ for the $\frac{1}{2}\langle 111\rangle$ dislocations and five zonal planes $\{100\}$, $\{110\}$, $\{210\}$, $\{310\}$, and $\{510\}$ planes for the $\langle 001\rangle$ junction dislocations. Accounting for cubic symmetries, for $\frac{1}{2}\langle 111\rangle$ dislocation it is sufficient to sample angles $-90^\circ \leq \theta \leq 90^\circ$, $0 \leq \phi \leq 30^\circ$ from an angular wedge that constitutes $\frac{1}{12}$ of the unit sphere of line vectors (see Fig. 1(b)), e.g. $(\bar{1}10)$, $(\bar{3}21)$ and $(\bar{2}11)$ planes of the [111] zone at zonal angles $\phi = \{0^\circ, \sim 19^\circ, 30^\circ\}$, respectively. Likewise for the $\langle 001\rangle$ dislocation it is sufficient to sample angles $-90^\circ \leq \theta \leq 90^\circ$, $0 \leq \phi \leq 45^\circ$ from an angular wedge that constitutes $\frac{1}{8}$ of the unit sphere of line vectors, e.g. planes $(\bar{1}00)$, $(\bar{5}10)$, $(\bar{3}10)$, $(\bar{2}10)$ and $(\bar{1}10)$ at zonal angles $\phi = \{0^\circ, 11^\circ, \sim 18^\circ, \sim 27^\circ, \sim 45^\circ\}$, respectively. For each zonal plane, dipole energies were computed for 40 to 80 in-plane dislocation characters spanning the entire range of line orientation $\theta \in [-90^\circ, 90^\circ]$ thus amounting to hundreds of distinct dislocation orientations for each of the two dislocation types considered. To assess and minimize the errors, dislocation core energies were computed for each line orientation in rectangular periodic supercells of four different sizes. Altogether, counting all dislocation orientations for both dislocation types, supercell dimensions and 13 interatomic potential models, about 10 thousand individual atomistic calculations were performed each producing a core energy value. In all cases, reference radius $r_c = b$ is used to document the core energies.

3 Results

Except where stated explicitly, core energies presented in this section were computed for BCC tungsten modelled with the EAM interatomic potential developed by Zhou et al. [20]. Quantitative differences notwithstanding, key findings reported here for this particular model are representative of all five metals and all interatomic potentials employed in this work (see Section 5 for core energy data computed for all 13 interatomic potentials).

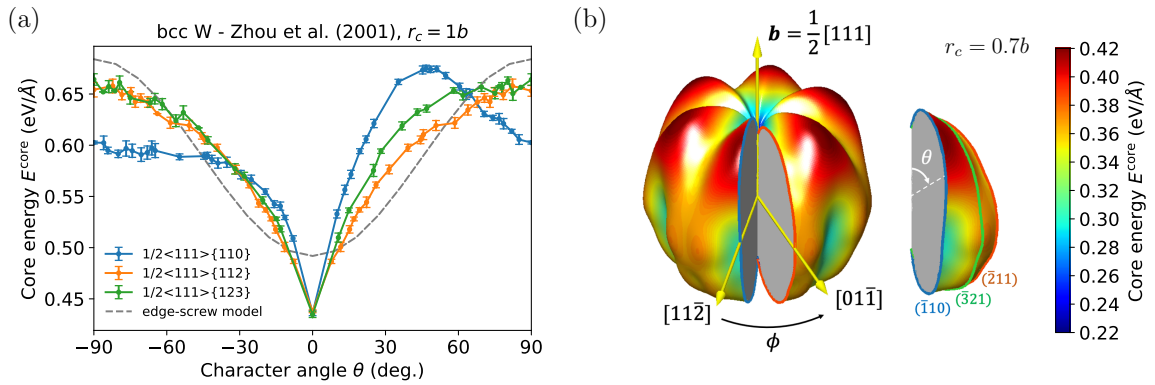

Figure 1: Core energy of a $\frac{1}{2}\langle 111\rangle$ dislocation in BCC tungsten. (a) Core energies as a function of zonal plane and character angle θ for $r_c = 1b$. Core energy values are averages over values computed in supercells of four different sizes (dipole separation distances). Each error bar is the standard error from the corresponding average. The dashed line is the least square fit of the edge-screw model (Eq. (8)) to the core energy data computed for all character angles and all three zonal planes. Inversion symmetry of the BCC lattice limits the range of distinct dislocation character angles to $-90^\circ \leq \theta < +90^\circ$. (b) 3D polar plot of core energy with the pole aligned along the Burgers vector. A slightly different value of the reference radius $r_c = 0.7b$ was used to sharpen the features of the core energy function plotted on the unit sphere (ϕ, θ) of dislocation orientations, where $0 \leq \phi < 360^\circ$ is the zonal angle, and θ is the character angle folded into $0 \leq \theta < 180^\circ$. The cutout slice is a symmetry-irreducible zone $0 \leq \phi < 30^\circ$ containing exactly one plane for each of the {110}, {112} and {123} families of zonal planes.

3.1 $\frac{1}{2}\langle 111\rangle$ dislocations

Dislocation core energies computed for the $\frac{1}{2}\langle 111\rangle$ dislocations are shown in Fig. 1(a) as functions of character angle θ for three zonal (glide) planes. First the energies of properly oriented dislocation dipoles were computed using methods described in the preceding section. Then dislocation core energies were extracted using elastic constants reported in Table 1 and referenced at $r_c = 1b$. Core energy of the screw dislocation orientation presents itself as a sharp minimum – a cusp – and is the same in all three planes within narrow error bars: $0.4361 \pm 0.0029\,\mathrm{eV/Å}$ on the $(\bar{1}10)$ plane, $0.4379 \pm 0.0017\,\mathrm{eV/Å}$ on the $(11\bar{2})$ plane, and $0.4347 \pm 0.0034\,\mathrm{eV/Å}$ on the $(1\bar{3}2)$ plane. Given that by the very definition of a screw dislocation its Burgers vector $\boldsymbol{b}$ is parallel to the line orientation vector $\boldsymbol{\xi}$, the cross product of the two vectors is zero meaning that for a screw no geometric glide (zonal) plane is defined. That core energies computed for the screw line orientation in supercells of three different geometries are the same is a good test on the accuracy and consistency of our computational workflow.

Away from the screw, dependence of the core energy on the in-plane character angle is different in the $(\bar{1}10)$, $(11\bar{2})$, and $(1\bar{3}2)$ planes. The core energy rises monotonically from the screw to the edge character in the $(11\bar{2})$ and $(1\bar{3}2)$ planes reaching their maxima (at $\theta = \pm 90^\circ$) of $0.6531 \pm 0.0061\,\mathrm{eV/Å}$ and $0.6642 \pm 0.0065\,\mathrm{eV/Å}$, respectively. Core energy

is perfectly symmetric with respect to the screw character ($\theta = 0$) in the $(11\bar{2})$ plane. In contrast, core energy in the $(\bar{1}10)$ plane is neither monotonic nor symmetric reaching a well defined maximum at $\theta \approx +50^\circ$. Variations of the core energy over in-plane characters and zonal planes are significant and, if ignored or accounted for incorrectly, would result in inaccurate predictions for total energies and forces on the dislocations. For example, the "edge-screw interpolation model" available in the DDD code ParaDiS [30] assumes that the core energy follows the same dependence on the character angle as the elastic energy in Eq. (2):

$$E_{\mathrm{e-s}}^{\mathrm{core}}(r_c) = \frac{\mu b^2}{4\pi}\left(\cos^2\theta + \frac{\sin^2\theta}{1-\nu}\right)\ln\left(\frac{r_c}{r_0}\right) \tag{8}$$

where r_0 is a free parameter that defines the amplitude of core energy variations between the edge and the screw characters. This isotropic model can be applied to the Zhou et al. [20] model of tungsten which is nearly elastically isotropic, with the Lamé constants of $\mu = 159.00$ GPa and $\nu = 0.28$. By varying r_0, the best fit of the screw-edge model (Eq. (8)) to dislocation core energies computed for all in-plane dislocation characters in all three planes is obtained at $r_0 = 0.435b$. The resulting best-fit model is shown as the dashed line in Fig. 1(a) and clearly fails to capture two of the most essential features of the core energy variations, namely the sharp cusp at $\theta = 0$ and the maximum at $\theta \approx 50^\circ$ in the $(\bar{1}10)$ plane. The same model also predicts the ratio of edge-to-screw core energies to always be the same and equal to $E_{\mathrm{e}}^{\mathrm{core}}/E_{\mathrm{s}}^{\mathrm{core}} = 1/(1-\nu)$ irrespective of r_c or r_0, which is generally not the case for core energies computed atomistically. On average, the best fit screw-edge model deviates from the computed core energies by $\sim 0.032\,\mathrm{eV/\AA}$. Discrepancies of such magnitude translate into spurious stress that has no physical origin but is certain to affect where and how dislocations move in a DDD simulation. If, instead of using the screw-edge model core energy variations of the kind reported here are ignored altogether, even greater spurious forces on dislocations will arise.

In Fig. 1(b) core energies of the $\frac{1}{2}[111]$ dislocation computed for the three families of zonal planes $\{110\}$, $\{112\}$ and $\{123\}$ are shown on the unit sphere (ϕ, θ) of all possible line orientations. Core energies in this figure are referenced at $r_c = 0.7b$ to sharpen the features of energy variations. The cutout slice is a symmetry-irreducible zone for zonal characters $0^\circ \leq \phi < 30^\circ$, bounded by the $(\bar{1}10)$ and $(\bar{2}11)$ zonal planes at 0° and 30°, respectively, and containing the $(\bar{3}21)$ plane at $\phi \approx 19^\circ$. In contrast to Fig. 1(a), here the character angle θ is defined in the range $[0^\circ, 180^\circ]$ such that the poles coincide with the screw orientation (the zonal axis), energy of which is independent of the zonal character. The full surface is obtained from the $\frac{1}{12}$ wedge (the cutout in Fig. 1(b)) by applying appropriate cubic symmetries.

Precise shapes of core energy variations shown in Fig. 1 are affected by the choice of reference radius r_c. For example, a reduction in r_c causes all core energies to decrease, but the reduction is greater for some dislocation characters than for others. Conversely, the maximum at $\theta \approx 50^\circ$ character in the $(\bar{1}10)$ zonal plane can be made to disappear by selecting a value of r_c greater than b. However two key characteristics that the screw-edge model fails to capture – specifically, the cusp at $\theta = 0$ and asymmetry in the $(\bar{1}10)$ plane – are robust. We note by reference to Section 5, that similar qualitative characteristics are observed in core energy variations in all 13 models of BCC metals employed in this

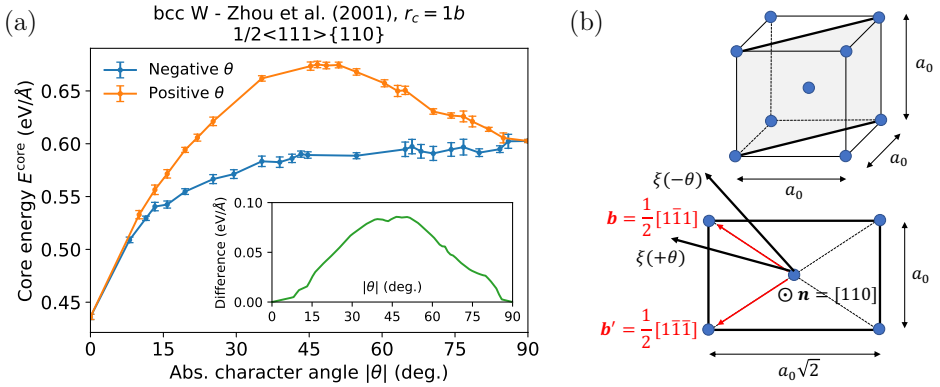

Figure 2: (a) Asymmetry of the core energy of a $\frac{1}{2}\langle 111\rangle\{\bar{1}10\}$ dislocation as a function of the character angle θ for a core radius $r_c = 1b$. The inset shows variations of the difference $E^{\text{core}}(\theta) - E^{\text{core}}(-\theta)$ in core energies between positive and negative character angles. (b) Schematic of the (110) plane in a BCC crystal with lattice parameter a_0. The asymmetry of dislocation lines $\boldsymbol{\xi}$ with positive $(+\theta)$ and negative $(-\theta)$ character angles with respect to the Burgers vector, e.g. $\boldsymbol{b} = \frac{1}{2}[1\bar{1}1]$, directly results from the crystallography of the (110) plane.

work. Data presented in Fig. 1 draws attention to previously unknown major variations in the core energy as a function of in-plane and, especially, zonal character. The same data motivates the need for more accurate descriptions of the core energy variations that can be transferred to accurate predictions of dislocation behavior in mesoscale simulations.

Among hundreds of dislocation orientations studied in this work, core energy variations in the $\{110\}$ zonal planes are most unusual. The same planes are also widely recognized as most important planes for BCC metal plasticity because this is where dislocations glide in BCC metals [18]. Fig. 2(a) is a re-plot of the same data for dislocation core energies in the $(\bar{1}10)$ plane of tungsten as in Fig. 1(a), but now focused on asymmetry with respect to the sign of the in-plane character angle θ. Core energies computed for $\theta > 0$ are systematically higher than core energies computed for $\theta < 0$ with the difference reaching its maximum of $0.0856\,\text{eV/Å}$ at $|\theta| \approx 50°$. The asymmetry results from the particular crystallography of the (110) plane in the BCC lattice, Fig. 2(b). The unit motif in the (110) plane is a centered rectangle with sides a_0 and $a_0\sqrt{2}$, where a_0 is the lattice parameter. As illustrated in the picture, distortions in relative atom positions in the dislocation core should be different for two line orientations $\boldsymbol{\xi}$ that form positive $(+\theta)$ and negative $(-\theta)$ angles with respect to the Burgers vector aligned with the diagonal of the rectangle, $\boldsymbol{b} = \frac{1}{2}[1\bar{1}1]$ in Fig. 2(b). Our convention here is to assign a positive sign to character angles for which the dislocation line vector $\boldsymbol{\xi}$ deviates from the Burgers vector $\boldsymbol{b}$ towards the second $\langle 111\rangle$ direction in the same plane (each $\{110\}$ plane contains two $\langle 111\rangle$ directions), that is towards the $\boldsymbol{b}' = \frac{1}{2}[1\bar{1}\bar{1}]$ direction in Fig. 2(b). For a dislocation with a positive character angle, the dislocation line runs between atom sites that are closer spaced than for a dislocation line with the same but negative character angle. Among two dislocation characters, core energy of the "positive" line orientation is thus expected to be higher.

In comparison to the $\{110\}$ and $\{112\}$ planes, core energies in the $\{123\}$ planes are nearly

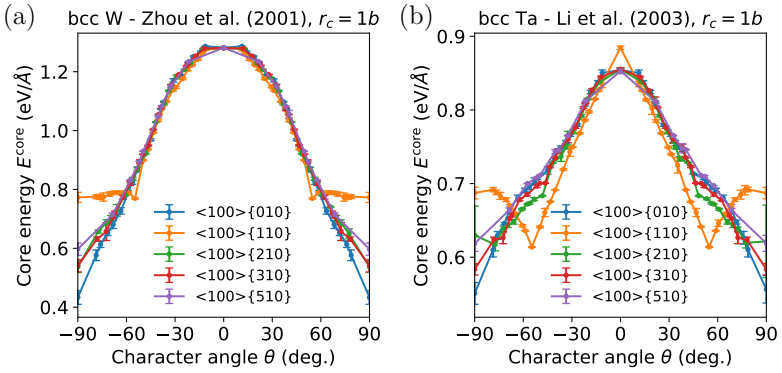

Figure 3: Core energy of $\langle 100 \rangle$ binary junctions as functions of the habit plane and character angle θ in (a) BCC W using the potential of Zhou et al. [20] (b) in BCC Ta using the potential of Li et al. [23]. Core energies are seen to increase monotonically from edge to screw characters in all habit planes, expect for the $\{110\}$ plane that shows a cusp at two dislocation line orientations dislocation line is aligned with two $\{111\}$ directions, i.e. for character angles of $\theta = \pm 54.74^\circ$.

but not exactly symmetric with respect to the character angle sign. The same is likely to be be the case for nearly all other planes of the $\langle 111 \rangle$ zone with the $\{112\}$ planes being the only exception; dislocation core energies in the $\{112\}$ planes are manifestly symmetric with respect to θ. This special symmetry arises because only in a $\{110\}$ zonal plane of the Burgers vector zone two dislocations with character angles $+\theta$ and $-\theta$ are "nearly exact" mirror images of each other with respect to the $\{110\}$ mirror plane perpendicular to the zonal $\{112\}$ plane. Meant by "nearly exact" here is that subsequent centro-symmetry inversion applied to just one of the two dislocations makes them exact mirror images.

3.2 $\langle 100 \rangle$ dislocations

In as-made and in pre-strained specimens of BCC metals, $\langle 100 \rangle$ dislocations are observed as a sizable minority to the ubiquitous $\frac{1}{2}\langle 111 \rangle$ dislocations. So far, structure and core energy of $\langle 100 \rangle$ dislocations in BCC metals have received relatively little attention. $\langle 100 \rangle$ dislocations are regarded as products of reactions zipping together two or more $\frac{1}{2}\langle 111 \rangle$ dislocations [5], e.g. in a binary reaction $\frac{1}{2}[1\bar{1}1] + \frac{1}{2}[11\bar{1}] = [100]$. Here we focus on orientations of $\langle 100 \rangle$ dislocations that can result from such a reaction between two $\frac{1}{2}\langle 111 \rangle$ parent dislocations gliding either on $\{110\}$ or on $\{112\}$ planes. It turns out that, depending on mutual orientation of the glide planes of two $\frac{1}{2}\langle 111 \rangle$ dislocations, their product (junction) $\langle 100 \rangle$ dislocations can form only in five geometric glide planes: $\{010\}$, $\{110\}$, $\{210\}$, $\{310\}$, and $\{510\}$ planes. Again, the screw $\langle 100 \rangle$ dislocation is an exception since its geometric glide plane is undefined and it can in principle "glide" in any plane of its Burgers vector zone.

Core energies of $\langle 100 \rangle$ dislocations computed for Zhou et al. [20] interatomic potential model of tungsten and for Li et al. [23] interatomic potential model for tantalum are shown in Fig. 3. In all five zonal planes, dependence of the core energy on in-plane character angle θ is qualitatively different than what was observed for the $\frac{1}{2}\langle 111 \rangle$ dislocations. First, there is no marked cusp at the screw orientation ($\theta = 0$). In fact, at $r_c = b$ core energies of the

screw orientation is highest in all five zonal planes whereas core energies of edge dislocations are lowest in all zonal planes save $\{110\}$. Although the minima and the maxima can be inverted by increasing the reference radius, e.g. from $r_c = b$ to $r_c = 10b$, the screw character would still not be a sharp cusp of the kind observed for the $\frac{1}{2}\langle 111\rangle$ dislocations. Instead, a sharp cusp in the core energies of the $\langle 100\rangle$ dislocations appears at $\theta = \pm 54.74^\circ$ but only in the $\{110\}$ plane. These two character angles correspond to two close-packed $\langle 111\rangle$ crystallographic orientations in the $\{110\}$ planes (each $\{110\}$ plane contains two such $\langle 111\rangle$ orientations). The same two symmetric cusps in the $\{110\}$ planes are observed in all 13 interatomic potential models employed in this study, see Section 5. Although exact appearance of the two cusps can be modified to an extent by varying reference radius r_c, their presence is robust – the cusps will remain cusps irrespective of r_c. Among all planes of the $\langle 100\rangle$ zone, only $\{110\}$ planes contain $\langle 111\rangle$ directions which is likely why no cusps appear in any of the four remaining planes. Thus, for practical purposes it may generally be sufficient to break down core energies of $\langle 100\rangle$ dislocations into two groups of zonal planes (one group containing $\{110\}$ planes and the other all remaining planes), and document core energies for only one plane representative of each group, e.g. for $\langle 100\rangle\{010\}$ and $\langle 100\rangle\{110\}$ dislocations.

Special properties of $\langle 111\rangle$ line orientations have been previously reported for $\frac{1}{2}\langle 111\rangle$ dislocations. In addition to the screw dislocation which is obviously aligned with a $\langle 111\rangle$ direction, one other dislocation character in the $\{110\}$ plane was found to possess high Peierls stress in BCC tantalum [31]. The character angle of this second (after screw) special dislocation is $\mathrm{acos}(1/3) = 70.53^\circ$ which corresponds to the second $\langle 111\rangle$ direction in the $\{110\}$ that is not parallel to the Burgers vector. Sometimes referred to as a $M111$ dislocation (for "mixed-111"), our computed core energy data shows no discernible cusps near this line orientation for any of the 13 models of BCC metals used in our calculations. Nonetheless, the $\langle 111\rangle$ direction is clearly a special orientation for $\langle 100\rangle$ dislocations.

We note that, in all planes of the $\langle 100\rangle$ Burgers vector zone, a dislocation of character angle $-\theta$ can be obtained from a dislocation of character angle $+\theta$ by a 180° rotation around the Burgers vector. Subsequently, core energies of $\langle 100\rangle$ dislocations are symmetric with respect to the sign of the in-plane character angle θ in all zonal planes.

4 Dislocation core energy in non-singular elasticity theories

In the preceding two sections we discussed how to use classical continuum elasticity theory to extract and document dislocation core energies. Classical elasticity solutions for strain, stress and elastic energy density induced by a dislocation are singular, diverging asymptotically at close distances to the dislocation line. This divergence is a manifestation of the breakdown of fundamental assumptions of the linear elasticity theory and is conveniently side stepped by assigning finite core energy to a tube of radius r_c – the core – surrounding the line. Impossible to compute from the linear elasticity theory (in which it is infinite), such a core energy term is *a priori* unknown but can be calibrated against a suitable atomistic model. Alternative to the classical singular theory, versions of linear elasticity theory have been proposed in which core singularity is eliminated altogether and elastic energy integrated over the entire solid (including the dislocation line) becomes finite [10, 32]. However, even if finite, the resulting non-singular elastic energy does not represent the actual

core energy of a dislocation and still needs to be calibrated against an atomistic model. In this section we discuss how to use non-singular elasticity theories to partition and document dislocation core energies.

The logic is similar to the use of the singular theory discussed in Section 2. Given an atomistically computed total energy of a single dislocation or a dislocation dipole, an appropriate – isotropic or anisotropic – elasticity solution is used to compute the elastic energy component of the total energy in exactly the same geometry. Core energy is then whatever remains after subtracting the resulting elastic energy from the atomistic total energy. The only difference from the classical singular theory is that the non-singular elasticity solution for the elastic energy is now integrated over the entire volume containing the dislocation and no material is excluded. The workflow is most conveniently illustrated within the analytical non-singular theory developed by Cai et al. [10]. In their treatment the singularity in the dislocation core is eliminated by replacing the δ-functional distribution of the dislocation density characteristic of the singular elasticity theory, with a smooth distribution of the same density. Specifically, the density at each point on the line is now distributed using a spherically symmetric smoothing function $\tilde{\omega}(\boldsymbol{r}, a)$, the kernel. The kernel is normalized so that its volume integral is the same as for the δ-function, a unity.

It turned out possible to retain much of the concise analytical structure of the classical singular elasticity theory by employing a special kernel such that its double volume integral with vector $\boldsymbol{R}$ connecting two arbitrary field points becomes

$$R_a = \int\int d\boldsymbol{r'} d\boldsymbol{r''} \tilde{\omega}(\boldsymbol{r'}, a)\tilde{\omega}(\boldsymbol{r''}, a)|\boldsymbol{R} + \boldsymbol{r'} + \boldsymbol{r''}| = \sqrt{R^2 + a^2} \tag{9}$$

The same volume integral can be written symbolically as a double convolution $R_a = R * \tilde{\omega}(a) * \tilde{\omega}(a)$ or a single convolution $R_a = R * \omega(a)$ where $\omega(a) = \tilde{\omega}(a) * \tilde{\omega}(a)$ is the convolution of the smoothing core distribution $\tilde{\omega}(a)$ with itself. Here a is a parameter defining the spread or width of the spherically symmetric distribution $\tilde{\omega}(\boldsymbol{r}, a)$. Whereas kernel $\tilde{\omega}$ can be written in an analytical form only in the Fourier space, real space expression for ω leading to the elegant replacement $R \to R_a = \sqrt{R^2 + a^2}$ is [10]:

$$\omega(\boldsymbol{R}, a) = \frac{15}{8\pi a^3 \left[(R/a)^2 + 1\right]^{7/2}}, \quad R = \|\boldsymbol{R}\| \tag{10}$$

The non-singular model based on kernel in Eq. (10) was recently used to extract core energies of dislocations in various FCC metals and parametrize mesoscale DDD simulations [16, 17].

The same non-singular theory yields the following compact solution for the elastic energy of a dislocation dipole (see A) which is nearly the same as the corresponding solution of the classical singular theory (see Eq. (6)):

$$E_{\rm ns}^{\rm prm}(a) = \frac{\mu}{2\pi}(\boldsymbol{b}\cdot\boldsymbol{\xi})^2\left[\ln\left(\frac{R_a}{a}\right)+\frac{1}{2}-\frac{1}{2}\frac{a^2}{R_a^2}\right] + \frac{\mu}{2\pi(1-\nu)}(\boldsymbol{b}\times\boldsymbol{\xi})\cdot(\boldsymbol{b}\times\boldsymbol{\xi})\ln\left(\frac{R_a}{a}\right) + \frac{\mu}{2\pi(1-\nu)}\frac{1}{R_a^2}\left[(\boldsymbol{b}\times\boldsymbol{\xi})\cdot\boldsymbol{R}\right]^2 \tag{11}$$

The core energy can be extracted as half of the difference between the energy of the same dipole computed atomistically and the above solution. Similar to singular theory, parameter a is to be used here in place of r_c as a reference to document core energies $E^{\rm core}(a)$. Alternatively, core energies extracted and documented using the classical isotropic model at r_c can be converted into core energies usable within the non-singular elasticity and vice versa as follows

$$E_{\rm ns}^{\rm core}(a) = E_{\rm iso}^{\rm core}(r_c) + \frac{\mu}{4\pi}(\boldsymbol{b}\cdot\boldsymbol{\xi})^2\left[\ln\left(\frac{a}{r_c}\right)-\frac{1}{2}\right] + \frac{\mu}{4\pi(1-\nu)}(\boldsymbol{b}\times\boldsymbol{\xi})\cdot(\boldsymbol{b}\times\boldsymbol{\xi})\ln\left(\frac{a}{r_c}\right)+\mathcal{O}\left(\frac{a^2}{R^2}\right) \tag{12}$$

Fig. 4(a) compares core energies of $\frac{1}{2}\langle 111\rangle$ dislocations in the $\{110\}$ zonal plane in tungsten extracted using the classical singular elasticity described in Section 2 and using the non-singular isotropic elasticity described above, both with Lamé constants of $\mu = 159.00$ GPa and $\nu = 0.28$. Within the classical elasticity core energies were extracted using Eq. (6) with $r_c = b$ whereas within the non-singular elasticity Eq. (11) with $a = b$ was used for the purpose. As expected from Eq. (12), core energies extracted using two different methods differ quantitatively, although for our particular choice $r_c = a = b$ two core energies of the same edge dislocation happen to be nearly exactly the same. The difference between core energies of the screw and edge dislocations is greater within the non-singular theory. Furthermore, the maximum seen in the singular theory near 50° character angle disappears and asymmetry with respect to the character angle, while still there, appears to be less pronounced in the non-singular theory.

In the case of non-singular anisotropic elasticity, no closed-form analytical solution similar to the one above is available. However elastic energy of a dislocation dipole can be computed numerically using a spectral method [33, 34]. First, a kernel $g(\boldsymbol{x})$ is used to spread the initially singular Nye's tensor field $\boldsymbol{\alpha}^s(\boldsymbol{x})$ of two dislocations over a discrete grid in a periodic supercell

$$\boldsymbol{\alpha}^{\rm ns}(\boldsymbol{x}) = g(\boldsymbol{x}) * \boldsymbol{\alpha}(\boldsymbol{x}) \tag{13}$$

The convolution can be performed first in real space and then transformed to the reciprocal space or directly in the reciprocal space using fast Fourier transform (FFT). Solution for the non-singular stress field induced by the dislocation dipole is readily obtained in the reciprocal $\boldsymbol{k}$-space by multiplying the non-singular source field and the appropriate Green's operator $\boldsymbol{\Gamma}$ for anisotropic elasticity available in a closed form in the $\boldsymbol{k}$-space [33, 34]:

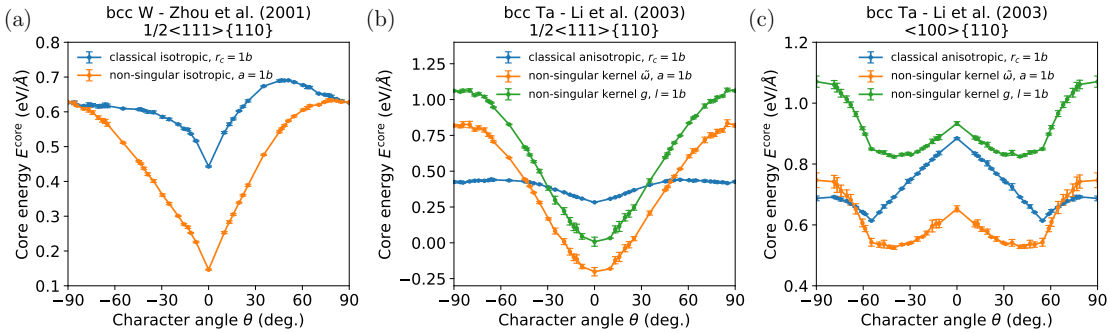

Figure 4: Examples of core energies extracted using different treatments of the elastic energy. (a) Comparison of the core energy in BCC W for the interatomic potential of Zhou et al. [20], extracted using classical isotropic elasticity (Eq. (6)) for $r_c = b$ and non-singular isotropic elasticity (Eq. (11)) with $a = 1b$ ($\mu = 159.00$ GPa, $\nu = 0.28$). (b) Comparison of the core energy in BCC Ta using the interatomic potential of Li et al. [23], extracted using classical anisotropic elasticity for $r_c = b$, anisotropic elasticity with the isotropic non-singular kernel in Eq. (10) for $a = b$, and anisotropic elasticity with the cubic non-singular kernel in Eq. (16) for $l = b$ ($C_{11} = 248.92$ GPa, $C_{12} = 144.27$ GPa, $C_{44} = 86.53$ GPa). (c) Same as in (b) but for the $\langle 100 \rangle \{110\}$ dislocation.

$$\boldsymbol{\sigma}^{\mathrm{ns}}(\boldsymbol{k}) = \boldsymbol{\Gamma}(\boldsymbol{k})\boldsymbol{\alpha}^{ns}(\boldsymbol{k}) \tag{14}$$

The total elastic energy induced by the dipole is then computed as the integral of the resulting stress field solution over the $\boldsymbol{k}$-space grid of the periodic supercell:

$$E^{\mathrm{dipole}} = E^{\mathrm{prm}} + E^{\mathrm{img}} = \frac{1}{2}\int_V S_{ijkl}\sigma_{ij}^{\mathrm{ns}}(\boldsymbol{k})\sigma_{kl}^{\mathrm{ns}}(\boldsymbol{k})d\boldsymbol{k} \tag{15}$$

where $\boldsymbol{S}$ is the tensor of elastic compliances. The so-computed elastic energy contains the primary and the image dipole contributions since the discrete Fourier transform is defined in 3D periodic boundary conditions and thus naturally accounts for both.

The spectral method can employ any appropriate non-singular kernel, e.g. the cloud-in-cell kernel used in [34] or the non-singular kernel introduced in [32] with its particularly simple analytical form for cubic crystals

$$g(\boldsymbol{k}) = \left[1 + l^2k^2\right]^{-1} \tag{16}$$

where l is a length parameter defining the spread of the non-singular Burgers distribution in real space. The non-singular kernel $\tilde{\omega}(\boldsymbol{x}, a)$ defined earlier in the context of the isotropic non-singular theory [10] can be also used for the same purpose. In the $\boldsymbol{k}$-space this kernel is simply $\tilde{\omega}(\boldsymbol{k}, a) = \sqrt{\omega(\boldsymbol{k}, a)}$, where $\omega(\boldsymbol{k}, a)$ is the Fourier transform of the distribution in Eq. (10). As a test, we verified that the energy of a dislocation dipole computed numerically for an isotropic solid with kernel $\tilde{\omega}(\boldsymbol{k}, a)$ using Eq. (15) is equal to the energy of the same dipole computed using the analytical expression in Eq. (11).

Fig. 4(b) compares core energies of the $\frac{1}{2}\langle 111 \rangle$ dislocations in the $\{110\}$ zonal plane computed for the Li et al. [23] model of tantalum and extracted using the classical singular

anisotropic elasticity (Eq. (7)) and two anisotropic non-singular models with kernels defined in Eq. (10) and Eq. (16). With the choice $r_c = a = l = b$, the core energies differ significantly. In particular, core energies extracted using two non-singular models vary over a significantly wider range compared to the same core energies extracted using the singular elasticity. At the same time, core energies extracted using two non-singular models appear to be different only by a constant. Within the non-singular model with kernel $\tilde{\omega}$, the core energies become negative for a range of dislocation characters near the screw. To avert possible numerical instabilities caused by negative core energies, a larger value for parameter a is advised. A similar comparison is given in Fig. 4(c) for the core energies of $\langle 100 \rangle$ dislocation in the $\{110\}$ zonal planes for the same model of tantalum. With the same choice for the reference parameters $r_c = a = l = b$, the core energies differ substantially among the three models and yet all three show marked cusps at the $\langle 111 \rangle$ line orientation. That the cusp appears in all three elasticity models suggests the same cusp it is not a property of any particular elasticity model but reflects a special core structure of the $\langle 100 \rangle$ dislocations aligned along the close-packed $\langle 111 \rangle$ directions of the BCC lattice.

Three comparisons in Fig. 4 illustrate that, even though reference length parameters r_c, a, and l have different meanings within three different elasticity models and thus the resulting core energies differ significantly when viewed side by side, any one of the three can be consistently applied for partitioning and documenting the core energies. Which particular method should be employed is defined by the intended use of extracted core energies. For example, if the non-singular cloud-in-cell anisotropic model [34] with grid spacing d is the intended application, values of the core energies should be calibrated with respect to the same cloud-in-cell kernel and at the same grid spacing d as intended for subsequent DDD simulations. It is of course not necessary to repeat atomistic calculations to extract dislocation core energies each time a different elasticity model or a different reference length parameter is used. Instead, when both models are analytical a formula of the kind shown in Eq. (12) can be used to convert core energies from one model to the other. When one or both models are numerical, conversion energies can be computed and added when necessary or pre-tabulated in advance for subsequent use.

5 Dislocation core energies for BCC metals W, Ta, V, Mo and α-Fe

This section reports core energies calculated for all five BCC metals studied in this work, see Table 1. Core energies were extracted and documented using the classical singular anisotropic elasticity theory at the reference core radius $r_c = 1b$. The resulting core energies for the $\frac{1}{2}\langle 111 \rangle$ dislocation are shown Fig. 5 as functions of the character angle θ in the same zonal planes discussed in Section 3. For clarity and following the results presented in §3.2, core energies in only two of the five zonal planes are shown in Fig. 6 for the $\langle 100 \rangle$ junction dislocations. We note that despite obvious variations from one model potential to another, all essential features discussed in Section 3 are observed across all BCC metals and interatomic potentials studied here. In particular, asymmetry of the core energy with respect to the character angle of the $\frac{1}{2}\langle 111 \rangle$ dislocations in the $\{110\}$ zonal planes is observed in all models as are the distinct cusps at the $\theta = \pm 54.74^\circ$ character of the $\langle 100 \rangle$

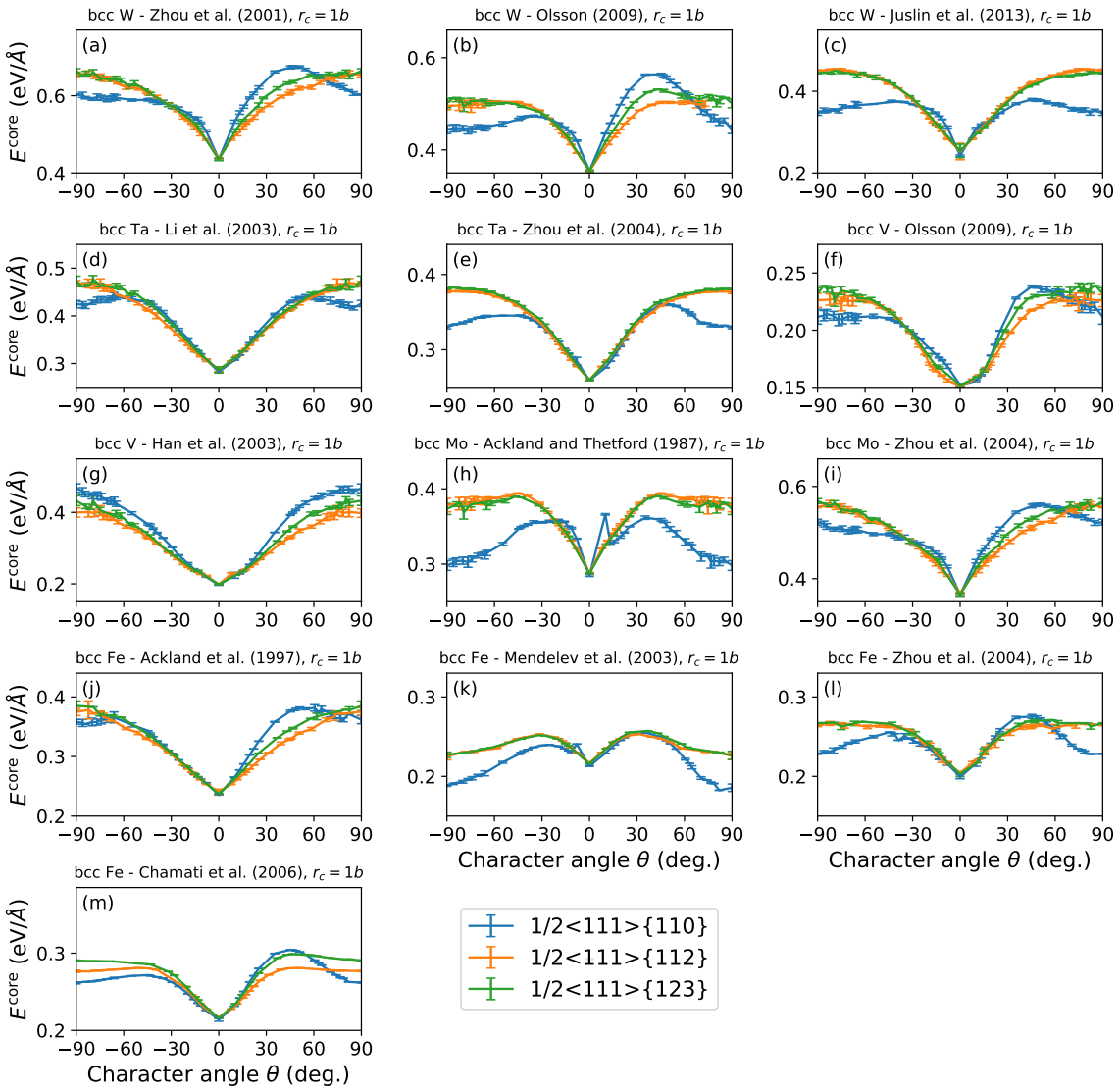

Figure 5: Core energies for the $\frac{1}{2}\langle 111\rangle$ dislocation extracted for all interatomic potentials considered in this work, see Table 1. Values of the core energies are plotted for the classical anisotropic elasticity model with cut-off core treatment at $r_c = 1b$. (a) BCC W, Zhou et al. [20], (b) BCC W, Olsson [21] (c) BCC W, Juslin et al. [22], (d) BCC Ta, Li et al. [23], (e) BCC Ta, Zhou et al. [24], (f) BCC V, Olsson et al. [21], (g) BCC V, Han et al. [25], (h) BCC Mo, Ackland and Thetford [26], (i) BCC Mo, Zhou et al. [24], (j) BCC α-Fe Ackland et al. [27], (k) BCC α-Fe, Mendelev et al. [28], (l) BCC α-Fe, Zhou et al. [24] and (m) BCC α-Fe, Chamati et al. [29].

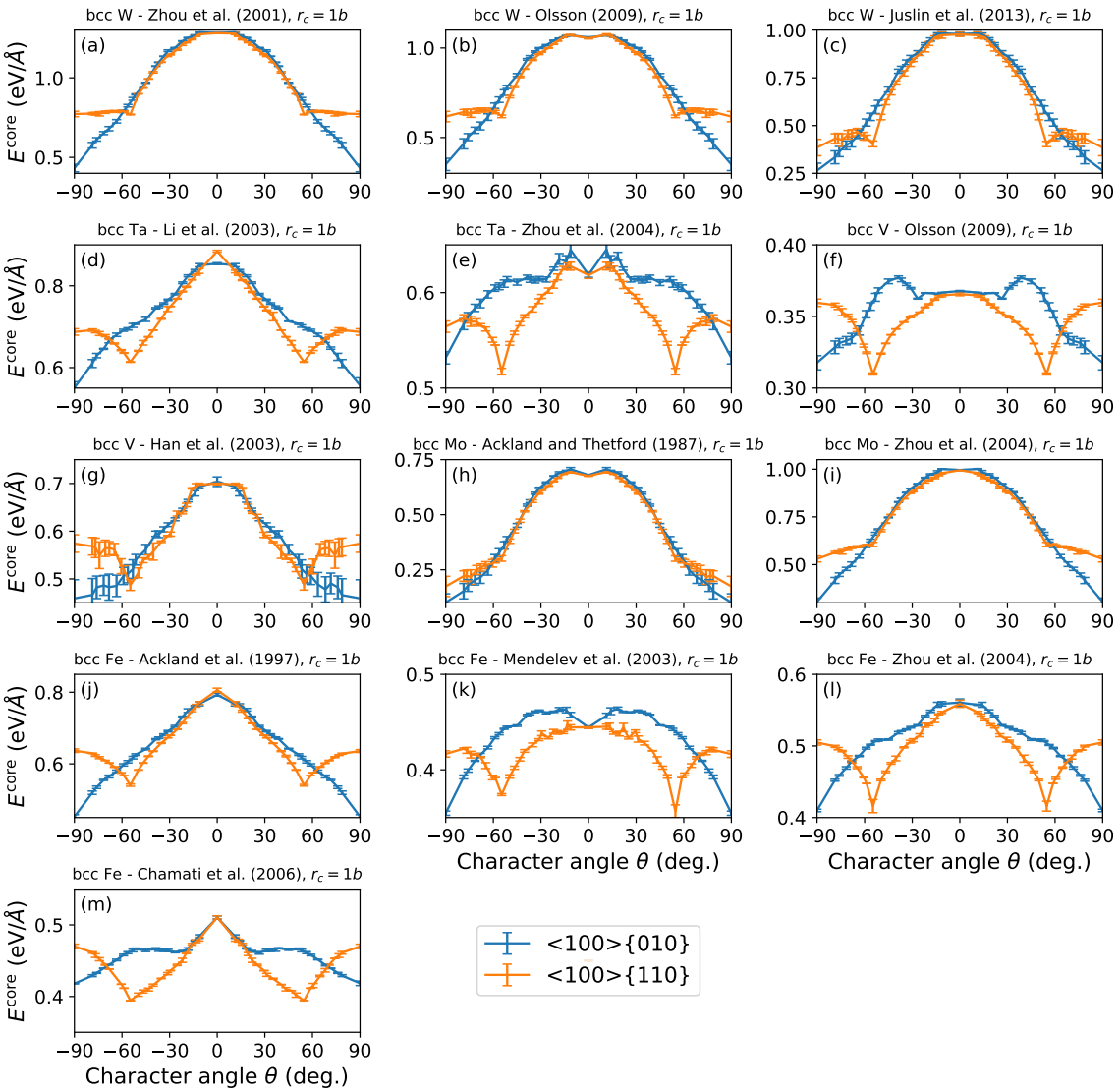

Figure 6: Core energies for the $\langle 100 \rangle$ dislocation extracted for all interatomic potentials considered in this work, see Table 1. Values of the core energies are plotted for the classical anisotropic elasticity model with cut-off core treatment at $r_c = 1b$. (a) BCC W, Zhou et al. [20], (b) BCC W, Olsson [21] (c) BCC W, Juslin et al. [22], (d) BCC Ta, Li et al. [23], (e) BCC Ta, Zhou et al. [24], (f) BCC V, Olsson et al. [21], (g) BCC V, Han et al. [25], (h) BCC Mo, Ackland and Thetford [26], (i) BCC Mo, Zhou et al. [24], (j) BCC α-Fe Ackland et al. [27], (k) BCC α-Fe, Mendelev et al. [28], (l) BCC α-Fe, Zhou et al. [24] and (m) BCC α-Fe, Chamati et al. [29].

dislocations in the {110} zonal planes. These two characteristics appear to universal across the BCC crystallography class. For some potentials, we also note minor cusps at other line orientations. These are likely to result from incomplete relaxation of the atomic configurations, possibly due to the presence of metastable states previously reported for some of the interatomic potentials.

To facilitate wider use of the methods developed here and of the core energies computed in this study, we assembled a set of python scripts used here to extract the core energies and compiled all resulting core energies into a database available for downloads. Note also that our approach here is to compute and document core energies for a large number of available interatomic potentials which, in addition to testing our methods and computational workflow, serves to identify results that are robust with respect to potentials we employ here and to provide a measure of variability in core energy predictions over potentials currently available. To select a potential for a particular application, we recommend to take advantage of the extensive potential database available in the OpenKIM project [35], which includes numerous tools to compute and compare properties across all interatomic potentials available in the repository, and against *ab-initio* reference calculations. In particular, the user can compare potentials available in OpenKIM in terms of their performance on properties deemed relevant for the application of interest, such as elastic constants, generalized stacking fault energies and such, for dislocation core predictions. Thus, to further assist the reader in extracting dislocation core energies for material models and dislocations other than ones reported here, our methods are being integrated under the OpenKIM framework into an automated workflow for managing and controlling all the required calculations [36]. With this, the user will be able to select a most appropriate interatomic potential from the database and directly calculate the corresponding dislocation core energies values following the methodology presented in our work.

6 Discussion and summary

In this paper we present a set of methods that constitute an accurate and efficient workflow for computing dislocation core energies. Two essential elements of the work flow are: (1) atomistic calculations required to obtain an accurate value of the excess energy in the standard configuration of a dislocation dipole in a 3D-periodic supercell and (2) calculations of elastic energy terms required to extract a dislocation core energy from the computed excess atomistic energy. Several forms of the elastic energy terms are given suitable for a variety of applications to elastically isotropic and anisotropic solids within both singular and non-singular variants of the linear elasticity theory. Which form to employ is dictated by the intended application. The isotropic elasticity solutions should be used only for crystals that are elastically isotropic such as tungsten. For most other crystals, anisotropic elasticity must be used. In either case, the same elastic constants must be employed both in extracting the core energies and in their use in subsequent calculations.

For energy partitioning to be accurate, dislocations of the primary dipole and their periodic images in the standard configuration should be placed at distances R greater than twice the physical width w of the dislocation core, $R \gg 2w$. The same condition should be satisfied in any subsequent re-use of extracted core energies for computing the total energy of dislocation configurations other than the standard dipole. Furthermore, transferability

of extracted core energies to curved dislocation configurations places a similar restriction on the curvature radius of the dislocation lines, $R \gg 2w$. The opposite limit of a high line curvature, $R \ll 2w$, such as at a node of a dislocation junction or at a cross-slip node, presents an interesting and important target for further study. In such configurations, further partitioning of the dislocation core energy into its "line" and "node" terms should be possible following the logic previously applied in partitioning the excess interfacial energy of a polycrystal into distinct contributions associated with grain boundaries and triple lines [37]. Here as there, exactly how to partition the core energy among lines and nodes can be arbitrary for as long as the total excess energy is preserved.

Our primary intention is to use our core energy data to accurately parameterize Discrete Dislocation Dynamics (DDD) models of BCC metals [30]. In this context, pre-computed core energies are used to accurately reproduce total excess energies defining forces on line segments in complex dislocation configurations evolving along the simulation trajectory. Even if core energies can be documented by reference to an arbitrary value of core radius r_c, care is advised in selecting r_c for use in DDD simulations. Although r_c can be selected smaller than even the physical diameter w of the non-linear core, such partitioning can result in negative core energies for some or all line orientations and, simultaneously, in excessively large elastic energies which may be prone to numerical instabilities in integrating equations of motion of dislocation line segments. Sensitivity of DDD simulations to accurate values of dislocation core energies should be greater whenever the elastic energy associated with the same dislocations is diminished. Such conditions are in place under high straining rates where dislocations are generated in high densities and form dense networks in which dislocations strongly screen (suppress) each other's strain fields [38]. In the opposite limit of low straining rates dislocations remain sparse and selecting r_c greater than w can be beneficial. For instance, by setting r_c to be a greater fraction of the dislocation spacing, part of the elastic energy can be subsumed into the core energy while still maintaining an acceptable level of accuracy in low-rate DDD simulations. Such re-balancing of dislocation energies from elastic to core reduces demands on spatial resolution of DDD simulations and can substantially increase their computational efficiency. Whichever reference length parameter is used, r_c, or a or l, its magnitude should be coordinated with the intended resolution of the DDD model to balance computational efficiency with accuracy.

In this computational study we extracted core energies of $\frac{1}{2}\langle 111\rangle$ and $\langle 100\rangle$ dislocations presenting a dense sample of the entire 2-space of dislocation line orientations. Considered as functions of line orientation, the resulting core energies exhibit distinct features, namely cusps and asymmetries, not accounted for in the core energy models presently in use. Core energies of $\frac{1}{2}\langle 111\rangle$ dislocations on $\{110\}$ planes are observed to be asymmetric with respect to the sign of the dislocation character angle: the asymmetry is traced to the specific crystallography of the BCC lattice. Core energies of $\langle 100\rangle$ dislocations on the $\{110\}$ planes exhibit similarly distinct cusps for line orientations corresponding to the closed-packed $\{111\}$ crystallographic directions, i.e. for character angles of $\theta = \pm 54.74^\circ$. These findings hold for all five BCC metals and 13 interatomic potential models examined in this study.

Acknowledgement

This work was performed under the auspices of the U.S. Department of Energy by Lawrence Livermore National Laboratory under contract DE-AC52-07NA27344 (NB, SA and VB). This work was partly supported by the US Department of Energy, Office of Basic Energy Sciences, Division of Materials Sciences and Engineering under Award No. DE-SC0010412 (WC).

A Non-singular energy of a dislocation dipole

Using the classical theory of elasticity, it can be shown that the elastic interaction energy between two dislocation loops can be expressed as [1]

$$\begin{aligned} W = &- \frac{\mu}{4\pi} \oint_C \oint_{C'} \nabla^2 R \, (\boldsymbol{b} \times \boldsymbol{b}') \cdot (d\boldsymbol{x} \times d\boldsymbol{x}') \\ &+ \frac{\mu}{8\pi} \oint_C \oint_{C'} \nabla^2 R \, (\boldsymbol{b} \cdot d\boldsymbol{x})(\boldsymbol{b}' \cdot d\boldsymbol{x}') \\ &+ \frac{\mu}{4\pi(1-\nu)} \oint_C \oint_{C'} (\boldsymbol{b} \times d\boldsymbol{x}) \cdot \boldsymbol{T} \cdot (\boldsymbol{b}' \times d\boldsymbol{x}') \end{aligned} \tag{17}$$

where $\boldsymbol{b}$ and $\boldsymbol{b}'$ are the Burgers vectors of loops C and C', respectively, $R = \sqrt{\boldsymbol{R} \cdot \boldsymbol{R}}$ is the norm of the radius vector $\boldsymbol{R}$ linking the positions on the two loops, whose spatial derivatives are given by

$$T_{ij} = \frac{\partial^2 R}{\partial x_i \partial x_j} = R_{,ij} = \left(\delta_{ij} - \frac{R_i}{R} \frac{R_j}{R} \right) / R \tag{18}$$

$$\nabla^2 R = R_{,kk} = \frac{2}{R} \tag{19}$$

In the non-singular theory [10], the Burgers vector is spread isotropically around the dislocation line. With this, the non-singular radius vector $R_a = \sqrt{R^2 + a^2}$ is conveniently defined, where a is the core width, and the non-singular interaction energy is obtained from Eq. (17) as

$$\begin{aligned} W_{\text{ns}} = &- \frac{\mu}{4\pi} \oint_C \oint_{C'} \nabla^2 R_a (\boldsymbol{b} \times \boldsymbol{b}') \cdot (d\boldsymbol{x} \times d\boldsymbol{x}') \\ &+ \frac{\mu}{8\pi} \oint_C \oint_{C'} \nabla^2 R_a (\boldsymbol{b} \cdot d\boldsymbol{x})(\boldsymbol{b}' \cdot d\boldsymbol{x}') \\ &+ \frac{\mu}{4\pi(1-\nu)} \oint_C \oint_{C'} (\boldsymbol{b} \times d\boldsymbol{x}) \cdot \boldsymbol{T}_a \cdot (\boldsymbol{b}' \times d\boldsymbol{x}') \end{aligned} \tag{20}$$

where

$$T_{a,ij} = \frac{\partial^2 R_a}{\partial x_i \partial x_j} = R_{a,ij} = \left(\delta_{ij} - \frac{R_i}{R_a} \frac{R_j}{R_a} \right) / R_a \tag{21}$$

$$\nabla^2 R_a = R_{a,kk} = \frac{2}{R_a} + \frac{a^2}{R_a^3} \tag{22}$$

When considering a dislocation dipole composed of two infinitely straight, parallel dislocation lines of opposite Burgers vector $\pm\boldsymbol{b}$, it follows from Eq. (20) that the elastic interaction energy per unit length of the dipole reduces to

$$\begin{aligned} E_{\mathrm{ns}}^{\mathrm{prm}} = & \frac{\mu}{2\pi}(\boldsymbol{b}\cdot\boldsymbol{\xi})^2 \left[\ln\left(\frac{R_a}{a}\right) + \frac{1}{2} - \frac{1}{2}\frac{a^2}{R_a^2}\right] \\ & + \frac{\mu}{2\pi(1-\nu)}(\boldsymbol{b}\times\boldsymbol{\xi})\cdot(\boldsymbol{b}\times\boldsymbol{\xi})\ln\left(\frac{R_a}{a}\right) \\ & + \frac{\mu}{2\pi(1-\nu)}\frac{1}{R_a^2}\left[(\boldsymbol{b}\times\boldsymbol{\xi})\cdot\boldsymbol{R}\right]^2 \end{aligned} \tag{23}$$

where $\boldsymbol{\xi}$ is the line direction of the dislocations, and $\boldsymbol{R}$ denotes the separation vector between both lines of the dipole.

When the separation vector is orthogonal to the glide plane of the dislocation (i.e. $\boldsymbol{R} \parallel (\boldsymbol{b}\times\boldsymbol{\xi})$), the interaction energy of the dipole in Eq. (23) bcomes:

$$E_{\mathrm{ns}}^{\mathrm{prm}}(\theta) = \frac{\mu b^2}{2\pi}\left[\left(\cos^2\theta + \frac{\sin^2\theta}{1-\nu}\right)\ln\left(\frac{R_a}{a}\right) + \left(\frac{\cos^2\theta}{2} + \frac{\sin^2\theta}{1-\nu}\right)\left(1 - \frac{a^2}{R_a^2}\right)\right] \tag{24}$$

where $\theta = \cos^{-1}\left(\boldsymbol{b}\cdot\boldsymbol{\xi}/\|\boldsymbol{b}\|\right)$ is the character angle of the dislocations.

For a screw dislocation dipole (i.e. $\theta = 0$), Eq. (24) reduces to

$$E_{\mathrm{ns}}^{\mathrm{prm,\,screw}} = \frac{\mu b^2}{2\pi}\left[\ln\left(\frac{R_a}{a}\right) + \frac{1}{2} - \frac{1}{2}\frac{a^2}{R_a^2}\right] \tag{25}$$

For an edge dislocation dipole (i.e. $\boldsymbol{b}\cdot\boldsymbol{\xi} = 0$) with separation vector orthogonal to the Burgers vector (i.e. $\theta = \frac{\pi}{2}$), Eq. (24) reduces to

$$E_{\mathrm{ns}}^{\mathrm{prm,\,edge}} = \frac{\mu b^2}{2\pi(1-\nu)}\left[\ln\left(\frac{R_a}{a}\right) + 1 - \frac{a^2}{R_a^2}\right] \tag{26}$$

References

[1] P. M. Anderson, J. P. Hirth, and J. Lothe, *Theory of dislocations*, ch. 3 and 4. Cambridge University Press, 2017.

[2] V. Bulatov and W. Cai, *Computer simulations of dislocations*, vol. 3. Oxford University Press on Demand, 2006.

[3] W. Cai, V. V. Bulatov, J. Chang, J. Li, and S. Yip, "Dislocation core effects on mobility," *Dislocations in solids*, vol. 12, pp. 1–80, 2004.

[4] R. Madec, B. Devincre, and L. Kubin, "From dislocation junctions to forest hardening," *Physical review letters*, vol. 89, no. 25, p. 255508, 2002.

[5] V. V. Bulatov, L. L. Hsiung, M. Tang, A. Arsenlis, M. C. Bartelt, W. Cai, J. N. Florando, M. Hiratani, M. Rhee, G. Hommes, T. G. Pierce, and T. D. de la Rubia, "Dislocation multi-junctions and strain hardening," *Nature*, vol. 440, no. 7088, pp. 1174–1178, 2006.

[6] R. B. Sills, N. Bertin, A. Aghaei, and W. Cai, "Dislocation networks and the microstructural origin of strain hardening," *Phys. Rev. Lett.*, vol. 121, p. 085501, 2018.

[7] C. H. Henager Jr and R. G. Hoagland, "Dislocation core fields and forces in fcc metals," *Scripta materialia*, vol. 50, no. 7, pp. 1091–1095, 2004.

[8] E. Clouet, L. Ventelon, and F. Willaime, "Dislocation core energies and core fields from first principles," *Phys. Rev. Lett.*, vol. 102, p. 055502, 2009.

[9] E. Clouet, "Dislocation core field. i. modeling in anisotropic linear elasticity theory," *Physical Review B*, vol. 84, no. 22, p. 224111, 2011.

[10] W. Cai, A. Arsenlis, C. R. Weinberger, and V. V. Bulatov, "A non-singular continuum theory of dislocations," *Journal of the Mechanics and Physics of Solids*, vol. 54, no. 3, pp. 561–587, 2006.

[11] D. Hull and D. Bacon, *Introduction to Dislocations (Fifth Edition)*. Oxford: Butterworth-Heinemann, 2011.

[12] W. Cai, V. V. Bulatov, J. Chang, J. Li, and S. Yip, "Anisotropic elastic interactions of a periodic dislocation array," *Phys. Rev. Lett.*, vol. 86, pp. 5727–5730, 2001.

[13] W. Cai, V. V. Bulatov, J. Chang, J. Li, and S. Yip, "Periodic image effects in dislocation modelling," *Philosophical Magazine*, vol. 83, no. 5, pp. 539–567, 2003.

[14] X. W. Zhou, R. B. Sills, D. K. Ward, and R. A. Karnesky, "Atomistic calculations of dislocation core energy in aluminium," *Phys. Rev. B*, vol. 95, p. 054112, 2017.

[15] J. Li, C.-Z. Wang, J.-P. Chang, W. Cai, V. V. Bulatov, K.-M. Ho, and S. Yip, "Core energy and peierls stress of a screw dislocation in bcc molybdenum: A periodic-cell tight-binding study," *Physical Review B*, vol. 70, no. 10, p. 104113, 2004.

[16] P.-A. Geslin, R. Gatti, B. Devincre, and D. Rodney, "Implementation of the nudged elastic band method in a dislocation dynamics formalism: application to dislocation nucleation," *Journal of the Mechanics and Physics of Solids*, vol. 108, pp. 49–67, 2017.

[17] Y. Hu, B. Szajewski, D. Rodney, and W. Curtin, "Atomistic dislocation core energies and calibration of non-singular discrete dislocation dynamics," *Modelling and Simulation in Materials Science and Engineering*, vol. 28, no. 1, p. 015005, 2019.

[18] C. R. Weinberger, B. L. Boyce, and C. C. Battaile, "Slip planes in bcc transition metals," *International materials reviews*, vol. 58, no. 5, pp. 296–314, 2013.

[19] A. Stukowski and K. Albe, "Extracting dislocations and non-dislocation crystal defects from atomistic simulation data," *Modelling and Simulation in Materials Science and Engineering*, vol. 18, no. 8, p. 085001, 2010.

[20] X. Zhou, H. Wadley, R. Johnson, D. Larson, N. Tabat, A. Cerezo, and A.K., "Atomic scale structure of sputtered metal multilayers," *Acta Materialia*, vol. 49, no. 19, pp. 4005 – 4015, 2001.

[21] P. A. Olsson, "Semi-empirical atomistic study of point defect properties in bcc transition metals," *Computational materials science*, vol. 47, no. 1, pp. 135–145, 2009.

[22] N. Juslin and B. Wirth, "Interatomic potentials for simulation of he bubble formation in w," *Journal of nuclear materials*, vol. 432, no. 1-3, pp. 61–66, 2013.

[23] Y. Li, D. J. Siegel, J. B. Adams, and X.-Y. Liu, "Embedded-atom-method tantalum potential developed by the force-matching method," *Phys. Rev. B*, vol. 67, p. 125101, 2003.

[24] X. Zhou, R. Johnson, and H. Wadley, "Misfit-energy-increasing dislocations in vapor-deposited cofe/nife multilayers," *Physical Review B*, vol. 69, no. 14, p. 144113, 2004.

[25] S. Han, L. A. Zepeda-Ruiz, G. J. Ackland, R. Car, and D. J. Srolovitz, "Interatomic potential for vanadium suitable for radiation damage simulations," *Journal of applied physics*, vol. 93, no. 6, pp. 3328–3335, 2003.

[26] G. Ackland and R. Thetford, "An improved n-body semi-empirical model for body-centred cubic transition metals," *Philosophical Magazine A*, vol. 56, no. 1, pp. 15–30, 1987.

[27] G. Ackland, D. Bacon, A. Calder, and T. Harry, "Computer simulation of point defect properties in dilute fe-cu alloy using a many-body interatomic potential," *Philosophical Magazine A*, vol. 75, no. 3, pp. 713–732, 1997.

[28] M. Mendelev, S. Han, D. Srolovitz, G. Ackland, D. Sun, and M. Asta, "Development of new interatomic potentials appropriate for crystalline and liquid iron," *Philosophical magazine*, vol. 83, no. 35, pp. 3977–3994, 2003.

[29] H. Chamati, N. Papanicolaou, Y. Mishin, and D. Papaconstantopoulos, "Embedded-atom potential for fe and its application to self-diffusion on fe (1 0 0)," *Surface Science*, vol. 600, no. 9, pp. 1793–1803, 2006.

[30] A. Arsenlis, W. Cai, M. Tang, M. Rhee, T. Oppelstrup, G. Hommes, T. G. Pierce, and V. V. Bulatov, "Enabling strain hardening simulations with dislocation dynamics," *Modelling and Simulation in Materials Science and Engineering*, vol. 15, no. 6, pp. 553–595, 2007.

[31] K. Kang, V. V. Bulatov, and W. Cai, "Singular orientations and faceted motion of dislocations in body-centered cubic crystals," *Proceedings of the National Academy of Sciences*, vol. 109, no. 38, pp. 15174–15178, 2012.

[32] G. Po, M. Lazar, N. C. Admal, and N. Ghoniem, "A non-singular theory of dislocations in anisotropic crystals," *International Journal of Plasticity*, vol. 103, pp. 1 – 22, 2018.

[33] R. Brenner, A. J. Beaudoin, P. Suquet, and A. Acharya, "Numerical implementation of static field dislocation mechanics theory for periodic media," *Philosophical Magazine*, vol. 94, no. 16, pp. 1764–1787, 2014.

[34] N. Bertin, "Connecting discrete and continuum dislocation mechanics: A non-singular spectral framework," *International Journal of Plasticity*, vol. 122, pp. 268 – 284, 2019.

[35] E. B. Tadmor, R. S. Elliott, J. P. Sethna, R. E. Miller, and C. A. Becker, "The potential of atomistic simulations and the knowledgebase of interatomic models," *Jom*, vol. 63, no. 7, p. 17, 2011.

[36] Y. Qian, N. Bertin, D. Karls, Y. Afshar, V. Bulatov, E. B. Tadmor, and D. Cereceda, "Dislocation core energy for cubic crystals at a set of dislocation core cutoff radii v000," 2020. https://doi.org/10.25950/e62bb99e.

[37] G. S. Rohrer, "Grain boundary energy anisotropy: a review," *Journal of materials science*, vol. 46, no. 18, pp. 5881–5895, 2011.

[38] N. Bertin and W. Cai, "Energy of periodic discrete dislocation networks," *Journal of the Mechanics and Physics of Solids*, vol. 121, pp. 133–146, 2018.